



Article

# The Effect of Viscous Air Damping on an Optically Actuated Multilayer MoS<sub>2</sub> Nanomechanical Resonator Using Fabry-Perot Interference

Yumei She <sup>1,2</sup>, Cheng Li <sup>1,2,\*</sup>, Tian Lan <sup>1,2</sup>, Xiaobin Peng <sup>1,2</sup>, Qianwen Liu <sup>1,2</sup> and Shangchun Fan <sup>1,2</sup>

<sup>1</sup> School of Instrumentation Science and Opto-electronics Engineering, Beihang University, Beijing 100191, China; sheymbh@163.com (Y.S.); lantian435@163.com (T.L.); 12171038@buaa.edu.cn (X.P.); liuqianwenok@163.com (Q.L.); shangcfan@buaa.edu.cn (S.F.)

<sup>2</sup> Science and Technology on Metrology and Calibration Laboratory, Beijing 100095, China

\* Correspondence: licheng@buaa.edu.cn; Tel.: +86-10-8231-6625

Academic Editor: Ho Won Jang

Received: 14 July 2016; Accepted: 30 August 2016; Published: 5 September 2016

**Abstract:** We demonstrated a multilayer molybdenum disulfide (MoS<sub>2</sub>) nanomechanical resonator by using optical Fabry-Perot (F-P) interferometric excitation and detection. The thin circular MoS<sub>2</sub> nanomembrane with an approximate 8-nm thickness was transferred onto the endface of a ferrule with an inner diameter of 125 μm, which created a low finesse F-P interferometer with a cavity length of 39.92 μm. The effects of temperature and viscous air damping on resonance behavior of the resonator were investigated in the range of −10–80 °C. Along with the optomechanical behavior of the resonator in air, the measured resonance frequencies ranged from 36 kHz to 73 kHz with an extremely low inflection point at 20 °C, which conformed reasonably to those solved by previously obtained thermal expansion coefficients of MoS<sub>2</sub>. Further, a maximum quality (*Q*) factor of 1.35 for the resonator was observed at 0 °C due to viscous dissipation, in relation to the lower Knudsen number of 0.0025~0.0034 in the tested temperature range. Moreover, measurements of *Q* factor revealed little dependence of *Q* on resonance frequency and temperature. These measurements shed light on the mechanisms behind viscous air damping in MoS<sub>2</sub>, graphene, and other 2D resonators.

**Keywords:** multilayer MoS<sub>2</sub> diaphragm; resonator; viscous air damping; Fabry-Perot interference

## 1. Introduction

Nanomechanical resonators have been employed as tools to measure force [1], mass [2], charge [3], and displacement [4] with exquisite sensitivity. Recently, two-dimensional (2D) crystals, such as graphene and molybdenum disulfide (MoS<sub>2</sub>), have been enabling a new class of atomically thin nanoelectromechanical systems (NEMS) for sensing and actuation functions [5] due to the vanishing of bending rigidity with decreasing thickness [6]. Among the 2D materials employed for the fabrication of these devices, graphene has drawn the most attention and has been extensively studied so far [7–10], because of its high strength, stiffness, and thermal conductivity along the basal plane. For example, Bunch et al. fabricated suspended single- and multi-layer graphene sheets over trenches and measured the fundamental frequency of 1 MHz to 170 MHz and a *Q* factor of 20 to 850 at room temperature and a pressure of <10<sup>−6</sup> Torr [7]. Additionally, a suspended graphene nanoribbon resonator with all-electrical high-frequency actuation and detection presented that *Q* factor increased with decreasing temperatures, reaching ~1 × 10<sup>4</sup> at 5 K [8]. Clamping graphene membranes on all sides can reduce the variation in resonance frequency and make the behavior more predictable [9]. Hence, Barton et al. measured circular graphene mechanical resonators of various diameters using optical excitation and detection, and obtained a *Q* factor as high as 2400 ± 300 for a resonator with a diameter of 22.5 μm at room temperature and a pressure of <6 × 10<sup>−3</sup> Torr [10].

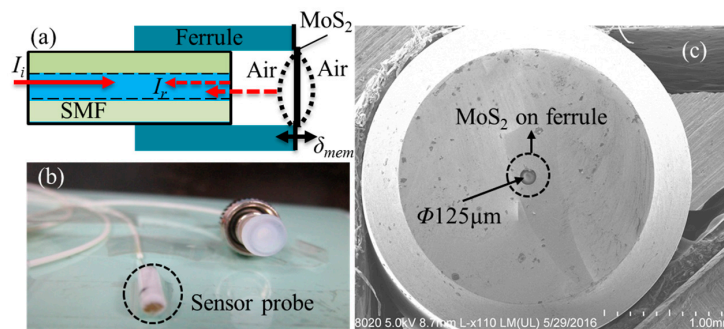
Similar to graphene, MoS<sub>2</sub> also has a hexagonal crystal structure [11] and demonstrates the potentially optical and optoelectronic applications [12]. Recent theoretical models using classical molecular dynamics simulation have demonstrated the possibility of lower intrinsic energy dissipation in MoS<sub>2</sub> [13]. Furthermore, ultralow areal mass density of 3.3 fg/μm<sup>2</sup>, high elastic modulus (~0.3 TPa), and an exceptional strain limit of 10%~12% [14] make it an attractive alternative to graphene, which typically has higher energy dissipation [15], especially in air damping due to a smaller thickness per unit layer and lower mass density [7]. For these reasons, much effort has been made to characterize the resonance behaviors of NEMS devices made of single-layer, few-layer, or multilayer MoS<sub>2</sub> films in a vacuum chamber using electrical or optical excitation at room temperature [16–19]. Lee et al. reported on the demonstration of MoS<sub>2</sub> nanodevices, where MoS<sub>2</sub> diaphragms as thin as 6 nm exhibited fundamental-mode nanomechanical resonances up to ~60 MHz in the very high frequency band, and frequency-*Q* factor products up to  $\sim 2 \times 10^{10}$  Hz [16]. Andres et al. fabricated suspended single-layer MoS<sub>2</sub> resonators, which behaved with resonance frequencies in between 10 and 30 MHz and *Q* factors in between 16 and 109 [17]. Then, Kramer et al. experimentally studied the effect of mechanical strain on the dynamics of thin 15-nm-thick MoS<sub>2</sub> nanodrum resonators with a diameter of 5 μm by using a piezoelectric bender to introduce strain [18]. Recently, Lee et al. further investigated  $\gamma$ -ray radiation effects on MoS<sub>2</sub> nanodrum resonators with diameters of 5–6 μm by using optical interferometric resonance readout, which vibrates at megahertz frequencies [19].

Accordingly, these experimental studies have significantly advanced the understanding of MoS<sub>2</sub> resonance behaviors. However, these approaches typically involve experiments where MoS<sub>2</sub> flakes in adhesive contact with a substrate are mechanically exfoliated by well-controlled forces, and the motions of these resonators are detected using an optical interferometer in vacuum pressure [15–19]. In fact, air damping is an important dissipation mechanism when nanomechanical resonators are operated in a moderate vacuum or near ambient, and resonance characteristics in air are completely different from those in a vacuum chamber [6]. Moreover, a complicated sample test process and specific measurement setups, such as a beam expander, a lens, a dichroic mirror, etc., are generally needed for the free-space optical excitation and detection technique used in the aforementioned literature. Hence, in this paper, from the viewpoint of MoS<sub>2</sub> device application instead of the aforementioned sample analysis, we fabricated a simple and miniature optical fiber Fabry-Perot (F-P) resonator with MoS<sub>2</sub> diaphragm to study the effect of viscous air damping on the F-P resonator in consideration of temperature changes, which contributes to the sensitive structural improvement and packaging design of F-P resonators. Moreover, we reported on experimental measurement of resonance behaviors of a chemically vapor deposited (CVD) MoS<sub>2</sub> diaphragm in air damping, which was suspendedly adhered to a zirconia (ZrO<sub>2</sub>) ferrule endface with a diameter of 125 μm, much larger than several microns in previously reported resonators [7–10,15–19]. Then, an F-P cavity made of the transferred MoS<sub>2</sub> diaphragm and a fiber end was easily formed to offer photothermal excitation and motion detection by using a simple F-P interference scheme rather than the complicated free-space optical actuation scheme mentioned above. Finally, thermal effects in the range of –10–80 °C were tested, which showed that resonance frequencies in contrast to *Q* factors strongly depended on the temperature due to thermal strain of the nanomembrane in viscous damping regime instead of previously described intrinsic damping or free molecule flow damping [5,20].

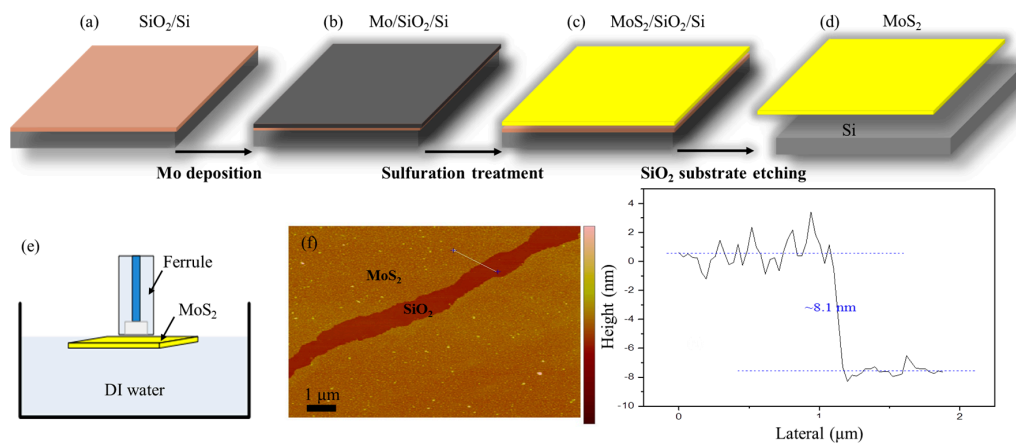
## 2. Fabry-Perot (F-P) Resonator Fabrication and Optical Actuation Model

Figure 1a,b show the schematic diagram and the physical picture of the presented F-P sensor probe that is comprised of a zirconia ferrule, a standard single mode fiber (SMF), and a multilayer MoS<sub>2</sub> diaphragm. The diaphragm, working as a light reflector made directly on the end of the SMF, is adhered to the zirconia substrate by van der Waals forces, and the initial cavity length of 39.92 μm between the fiber end and the ferrule endface is solved by an optical spectrum analyzer (AQ6370) to achieve the preferable reflected light intensity via a 1-μm resolution translation stage. As shown in

Figure 1c, the 125- $\mu\text{m}$  diameter hole is covered by the diaphragm. Then, the ferrule and the SMF are held together by an epoxy adhesive (3M<sup>®</sup>).



**Figure 1.** (a) Schematic diagram and (b) physical picture of the Fabry-Perot (F-P) sensor probe. (c) Microscopic image of the molybdenum disulfide ( $\text{MoS}_2$ ) diaphragm adhered to ferrule.



**Figure 2.** Fabrication process of the F-P cavity with a  $\text{MoS}_2$  membrane. (a)  $\text{SiO}_2/\text{Si}$  substrate. (b) Depositing Mo film onto the  $\text{SiO}_2/\text{Si}$  substrate. (c) Treating the  $\text{Mo}/\text{SiO}_2/\text{Si}$  assembly with sulfurization. (d) Separating  $\text{MoS}_2$  membrane from the  $\text{MoS}_2/\text{SiO}_2/\text{Si}$  assembly. (e)  $\text{MoS}_2$  membrane-covered fiber-capillary tip. (f) Thickness measurement of  $\text{MoS}_2$  membrane by atomic force microscopy (AFM).

The process for preparing the multilayer  $\text{MoS}_2$  membrane and transferring it onto the ferrule endface is depicted in Figure 2. Referring to Figure 2a,b, an atomically thin Mo membrane is deposited onto the  $\text{SiO}_2/\text{Si}$  substrate by an Anelva L-400 EK e-beam evaporation (Canon Anelva Corporation, Kanagawa, Japan). Then, the  $\text{Mo}/\text{SiO}_2/\text{Si}$  assembly is loaded into a CVD system operating at atmospheric pressure for sulfurization treatment as shown in Figure 2c. Note that the CVD system is firstly rinsed with Ar to purge the quartz tube with inert atmosphere, and the quartz tube reactor is then heated up to 750 °C with a rate of  $\sim 10$  °C/min under Ar atmosphere of 300 sccm. Besides, when the  $\text{Mo}/\text{SiO}_2/\text{Si}$   $\text{Mo}/\text{Si}$  assembly is transferred to the CVD system, it will be rinsed with ethyl alcohol and then dried with high purity nitrogen to avoid the possible surface contaminations. After the sulfurization, the  $\text{MoS}_2$  membrane will be grown on the  $\text{SiO}_2/\text{Si}$  substrate, and the  $\text{MoS}_2/\text{SiO}_2/\text{Si}$  assembly is then put in the cold zone of the CVD reactor to make fast cooling, which contributes to reducing the crystallinity of  $\text{MoS}_2$  [21]. Next, the grown  $\text{MoS}_2$  membrane can be separated from the substrate by etching away the  $\text{SiO}_2$  layer by hydrofluoric acid as shown in Figure 2d. The membrane is then transferred into de-ionized (DI) water. The following step is to suspend the membrane onto the endface of a ferrule. As illustrated in Figure 2e, the ferrule is moved down slowly toward the floating  $\text{MoS}_2$  membrane in DI water until it touches the membrane. The membrane is then attached to the endface of the ferrule by a van der Waals interaction. The  $\text{MoS}_2$  membrane-covered fiber-capillary tip

assembly is then left to dry in a cabinet at a room temperature, which is required to be below 50 °C for about half an hour. After water evaporation, the MoS<sub>2</sub> membrane is firmly stuck to the surface of the fiber-tip to form one light reflector of a sealed F-P microcavity. The magnified microscope image of MoS<sub>2</sub> diaphragm on the surface of the assembly is shown in Figure 1c. The exact thickness of MoS<sub>2</sub> membrane is confirmed by atomic force microscopy (AFM). From the height profile of the MoS<sub>2</sub>/SiO<sub>2</sub>/Si assembly in Figure 2f, the thickness of the fabricated MoS<sub>2</sub> membrane is determined to be ~8 nm.

According to the theory of multiple-beam interference, the interference intensity  $I_r$  in the fabricated F-P cavity in Figure 1a can be expressed as [22]

$$I_r = \frac{R_2 + \zeta R_1 + 2\sqrt{\zeta R_1 R_2} \cos \theta}{1 + \zeta R_1 R_2 + 2\sqrt{\zeta R_1 R_2} \cos \theta} I_i, \quad (1)$$

where  $R_1$  and  $R_2$  are, respectively, the reflectivities of MoS<sub>2</sub> membrane and the fiber end face.  $R_2$  is measured to be 2.5%, and  $I_i$  is the incident intensity.  $\zeta$  is the coupling coefficient of cavity length loss [23]. When ignoring the half-wave loss, the phase difference  $\theta$  between two adjacent beams in micro-air cavity can be written as

$$\theta = 4\pi L / \lambda, \quad (2)$$

where  $L$  is the length of F-P cavity, and  $\lambda$  is the wavelength of incident light. When a diaphragm-type F-P interferometer made of low-reflectivity mirrors is illuminated by a monochromatic light source, the response is a periodic function similar to a two-beam interferometer. Based on the thin-film optical theory and the Fresnel's equations for reflection and refraction [23], the reflectivity of MoS<sub>2</sub> film is measured to be ~0.89%. Thus, due to the lower reflectivities of the two F-P mirrors, Equation (1) can be simplified as

$$I_r = \left( R_2 + \zeta R_1 + 2\sqrt{\zeta R_1 R_2} \cos \theta \right) I_i, \quad (3)$$

It should be noted that applied optical excitation will cause the suspended MoS<sub>2</sub> diaphragm to vibrate due to thermal expansion and contraction. It is assumed that the displacement of diaphragm vibrating axially with simple harmonic motion is  $\delta_{mem} = A \sin(2\pi f t + \varphi)$ , where  $A$  is the amplitude,  $f$  is the frequency, and  $\varphi$  is the phase angle. As a result of the resonance motion of diaphragm,  $I_r$  can be rewritten as

$$I_r = \left[ R_2 + \zeta R_1 + 2\sqrt{\zeta R_1 R_2} \cos(\theta + 4\pi \delta_{mem} / \lambda) \right] I_i, \quad (4)$$

when the diaphragm does not vibrate,  $\delta_{mem} = 0$  and Equation (4) can then degenerate to Equation (3).

As seen from Equation (4), the reflected light intensity for F-P optical readouts shows a dependence on  $\delta_{mem}$ . Thus, the determination of resonance frequencies and  $Q$  factors is closely related with  $\delta_{mem}$ . In other words, the resonance characteristics of MoS<sub>2</sub> resonator as a light reflector can be measured by using an extrinsic F-P interferometric scheme. However, the  $\delta_{mem}$ -related incident light intensity should be adjusted to an appropriate range instead of an arbitrary higher value. Assuming the frequency of  $\delta_{mem}$  for the diaphragm is 53 kHz, which is defined as  $f_0$ . It can be inferred from the simulation results in Figure 3, where  $N \times f_0$  ( $N = 0, 1, \dots$ ) represents the  $N$ -order fundamental frequency, that  $I_r/I_i$  exhibits more obvious waveform distortions and frequency multiplication patterns with rolling energy distribution when the amplitude  $A$  of  $\delta_{mem}$  is set as larger values, such as 0.1~0.4  $\mu\text{m}$ . The phenomenon will result in nonlinear mode coupling and internal resonances related with complex energy transfer between various vibrational modes [15]. However, the discrete Fourier transform (DFT) amplitude of resonance response at  $f_0$  does not monotonically increase with  $A$  (Figure 3b, inset). In other words, merely a higher light intensity for obtaining the resonance with greater amplitude is not desirable. Therefore, appropriate excitation schemes, such as incident light intensity or signal modulation, should be considered properly for a certain material of resonator in view of its photothermal absorption property.

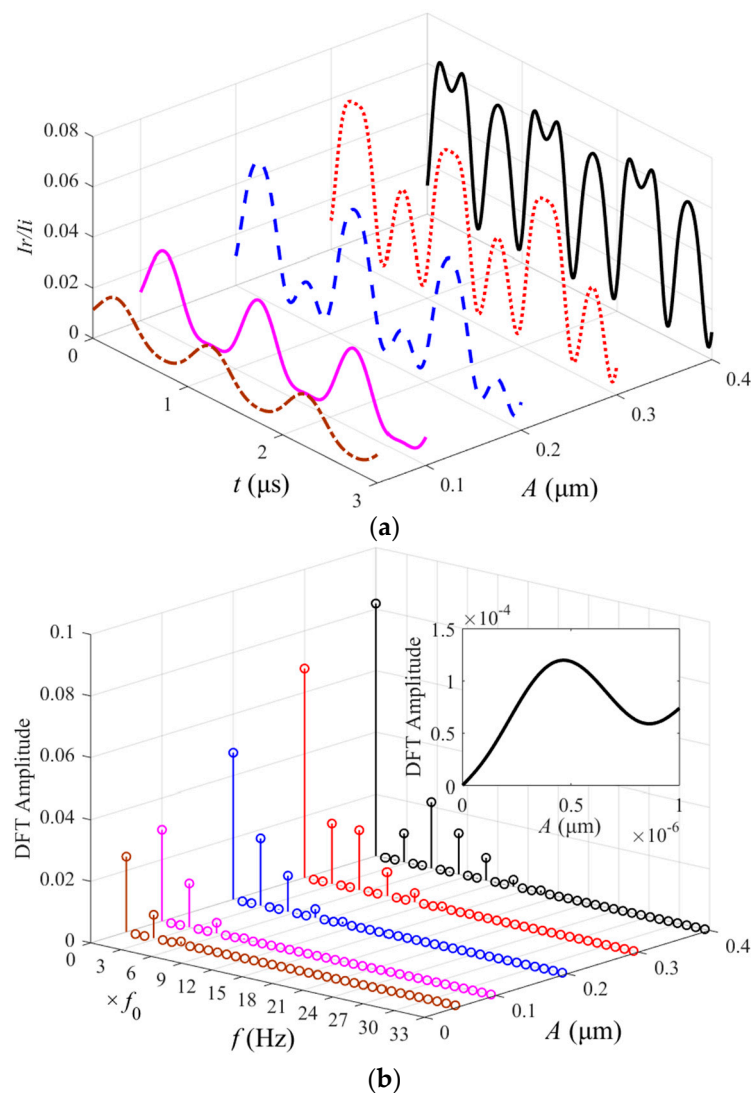


**Figure 3.** The effect of  $A$  on  $I_r/I_i$ . (a) Time-domain waveforms. (b) Frequency-domain waveforms. Inset: the discrete Fourier transform (DFT) amplitude- $A$  response at  $f_0$ .

### 3. Experiment and Analysis

Referring to Figure 4, to detect the resonance of the MoS<sub>2</sub> drum, we used an optical fiber F-P interferometric method rather than the free-space optical actuation one described previously [7,9,16–19]. Resonator motion was actuated using a 1550.12-nm amplitude-modulated distributed feedback (DFB) laser S (10 dBm output power) that excited motion through photothermal expansion and contraction of the MoS<sub>2</sub> diaphragm via an electro optical modulator (EOM) with power amplification. Then, resonator motion was monitored by another 1551.72 nm DFB laser R (10 dBm output power) reflecting from the resonator and the fiber tip. The light signals from the lasers S and R were optically coupled through a  $2 \times 1$  coupler, followed by input into the sensor probe via a 3-port circulator. The F-P interference was related with the reflected light intensity  $I_r$  when the resonator vibrated. After the separation of detection light with a wavelength of 1551.72 nm by an optical filter, the intensity was detected by a fast photodiode connected to a data acquisition unit (DAU). To estimate the effects of temperature on resonance characteristics, the F-P sensor probe and a thermocouple sensor were put inside a thermostat. The reference temperature was offered by a thermocouple thermometer (testo 925) with an accuracy of  $\pm (0.5 \text{ } ^\circ\text{C} + 0.3\%$  of measured value) in the range of  $-40 \text{ } ^\circ\text{C}$  to  $+900 \text{ } ^\circ\text{C}$  and an associated Type K thermocouple probe with an accuracy of Class 2 in the range of  $-60 \text{ } ^\circ\text{C}$

to +400 °C according to standard EN 60584-2. Considering the use of room temperature curable adhesive and common SMF, the tested temperature range was set as −10–80 °C with an interval of 10 °C. All resonance measurements were performed at atmospheric pressure, where viscous damping was found to be significant because the Knudsen number,  $K_n = \lambda_{MFP} / l_{device}$ , where  $\lambda_{MFP}$  is the mean free path of air molecules and  $l_{device}$  is MoS<sub>2</sub> device characteristic length, was solved as 0.0025~0.0034 in the temperature range mentioned above [5,24].

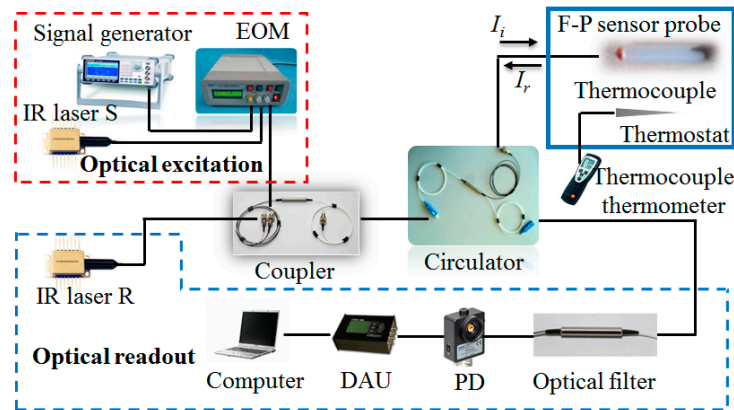


Figure 4. Schematic illustration of optical fiber F-P excitation and detection.

Since clamping the membranes on all sides made the distribution of higher resonance modes relative to the fundamental modes predictable [9], the resonance behavior of the clamped circular elastic MoS<sub>2</sub> diaphragm adhered to the ferrule endface as a function of temperature was examined. From Figure 5, the measured resonance frequency scales approximately as  $T^m$  where  $m = -5.348$  from −10 to 20 °C, and as  $T^n$  where  $n = 3.143$  from 20 to 80 °C. The frequency of the resonator at 20 °C achieves an extremely low value of 36 kHz. The origin of the frequency tunability with temperature is the change in tension in MoS<sub>2</sub> primarily due to the expansion/contraction of substrate and MoS<sub>2</sub> similar to the thermal expansion of graphene [25]. Thus, the total elastic strain  $\varepsilon(T)$  at a given temperature  $T$  in MoS<sub>2</sub> is approximately defined by

$$\varepsilon(T) = \int_{297}^T [\alpha_s(K) - \alpha_{mem}(K)] dK, \quad (5)$$

where  $\alpha_{mem}(K)$  and  $\alpha_s(K)$  are the coefficients of thermal expansion of substrate and MoS<sub>2</sub> [26], respectively. Since  $\varepsilon(T)$  is measured relative to the strain at room temperature (297 K), the change in tension in the membrane can be described as  $\Delta S(T) = Et\varepsilon(T) / (1 - \nu)$ , where  $E$ ,  $t$ , and  $\nu$  are the Young's modulus, thickness, and Poisson's ratio of MoS<sub>2</sub>, respectively. According to the membrane-to-plate behavior, the resonance frequency of the resonator in a cross-over regime can be calculated as [17]

$$f = \sqrt{f_{mem}^2 + f_{plate}^2} = \sqrt{\frac{0.146 S}{a^2 \rho t} + \frac{0.22Et^2}{\rho(1 - \nu^2)a^4}}, \quad (6)$$

where  $a$  is the radius of MoS<sub>2</sub>;  $\rho$  represents the mass density of MoS<sub>2</sub> with certain adsorbates;  $S$  is the tension in the membrane at  $T$ , which is equal to the sum of  $\Delta S(T)$  and the initial tension  $S_0$  at 297 K. Moreover, the resonance frequency shift of circular MoS<sub>2</sub> diaphragm in contact with air is approximately represented by [27]

$$f_{air} = f / \sqrt{1 + \rho_{air}a\Gamma / (\rho t)}, \quad (7)$$

where  $\rho_{air}$  is the density of air, and  $\Gamma$  is a non-dimensionalized added virtual mass incremental factor, which is a function of mode shapes and boundary conditions. For the fundamental resonant mode  $f_{0,1}$ ,

$\Gamma = 0.746$ . Accordingly, resonance frequency dispersion with temperature enables the estimation of  $\rho$  and  $S_0$  simultaneously by fitting measured frequencies based on the established continuum model. In this way, we estimated  $\rho = 10\rho_m$  and  $S_0$  to be  $0.054 \text{ N/m}$  for the fundamental mode, where  $\rho_m$  is the mass density of pure  $\text{MoS}_2$ . Similar to graphene resonators [9,10,25], the extra mass is attributed to resist residue and adsorbates from the fabrication and store process.

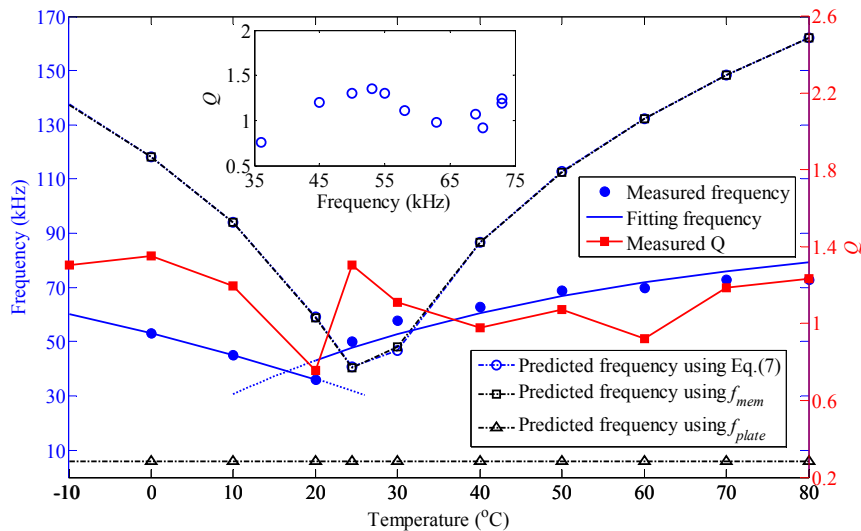


**Figure 5.** Resonance frequency  $f$  and  $Q$  factor as a function of temperature. Inset:  $Q$  factor verse  $f$ .

Referring to Figure 5 again, in comparison with the calculated fundamental frequencies ( $\circ$ , blue dashed line) using Equation (7), the variation of measured frequencies with temperature is well in agreement with the predicted results; however, there is a sharp frequency deviation up to  $63.47 \text{ kHz}$  between them, which is to a great extent caused by the presence of non-uniformly distributed adsorbates [17], the geometric imperfection such as microscopic wrinkles and surface-related effects [18], and the pressure change in the F-P cavity covered with  $\text{MoS}_2$  membrane due to thermal fluctuations [28]. It should be pointed out that there also appears to be an extremely low inflection point in the predicted spectrum represented by the symbol " $\circ$ " at  $24 \text{ }^\circ\text{C}$ , which deviates about  $4 \text{ }^\circ\text{C}$  from the measured inflection point. This shift of inflection point temperature possibly results from the non-uniformly distributed adsorbates and internal thermal deformation on the membrane. In addition, the resonance frequencies  $f_{air}$  are predicted based on Equation (7) using  $f_{mem}$ ,  $f_{plate}$ , and  $f$  in the membrane, plate, and cross-over regime, respectively. It is inferred from  $f_{air}$  plotted as by the symbols ' $\square$ ', ' $\Delta$ ', and ' $\circ$ ' that the resonator made of multilayer  $\text{MoS}_2$  should behave as a circular membrane dominated by initial pre-tension and thermal strain-dependent additional tension. Then, the  $Q$  factor can be extracted from the full width half-maximum of the Lorentzian resonance peak; nevertheless, there is no clear dependence of  $Q$  on temperature. The highest  $Q$  factor observed is  $\sim 1.35$  at  $0 \text{ }^\circ\text{C}$  for the resonator surrounding the air in tested temperature range, i.e., lower temperatures contribute to higher  $Q$  factors. The inset in Figure 5 shows that  $Q$  factor from  $\sim 0.7$  to  $\sim 1.35$  fluctuates around 1, which is weakly dependent on fundamental frequencies. However, the change of  $Q$  factor is quite significant in the limited test frequency ranging from  $35 \text{ kHz}$  to  $75 \text{ kHz}$ , which is in contrast to top-down fabricated microelectromechanical systems (MEMS) resonators, such as silicon nitride nanostrings, where a fitted linear relationship is achieved between  $Q$  factors from 17 to 600 and resonant frequencies from  $7 \text{ MHz}$  to  $206 \text{ MHz}$  by tuning operating pressures at room temperature [20]. Therefore, structural size is an essential factor determining the  $Q$  of the membrane [29], which is similar to the behavior of graphene resonator previously reported [10]. It is important to note that the experiments on resonance behavior versus temperature were repeated three times.

Figure 6a illustrates the resonance spectrum with an average fundamental frequency of  $f_0 = 53$  kHz and a maximum average value of  $Q = 1.35$  at  $0^\circ\text{C}$ . The resonator demonstrated little deviation from a harmonic response at this temperature due to the tensioned-membrane size effect in air damping. By averaging, two higher eigenmodes at  $1.68 f_0$  ( $\sim 89$  kHz) and  $2.26 f_0$  ( $\sim 120$  kHz) are found, which are in reasonable agreement with the predicted higher eigenmodes for a circular membrane ( $1.59 f_0$  and  $2.14 f_0$ ). The discrepancies between the measured values and the predicted values are also caused by non-uniform tensioned membrane and atmospheric adsorbates on the device. Furthermore, increasing optical power will further drive the resonator beyond the regime of harmonic oscillations as observed in Figure 6b, where the sampling frequency is set as 100 MHz. A gradually clear waveform distortion relative to a 50-kHz harmonic response is noticed when the driving power gain of EOM in Figure 4 is increased to 16.5 dB and then 21.5 dB from 15 dB, in agreement with the simulated responses shown in Figure 3b. This phenomenon features the nonlinear oscillation mode coupling effect along with rolling frequency multiplication components, which arises from the alternating tension in MoS<sub>2</sub> membrane due to higher vibration amplitude comparable to the membrane thickness, consistent with those recently reported for single-layer and multilayer MoS<sub>2</sub> resonators in [15,17].

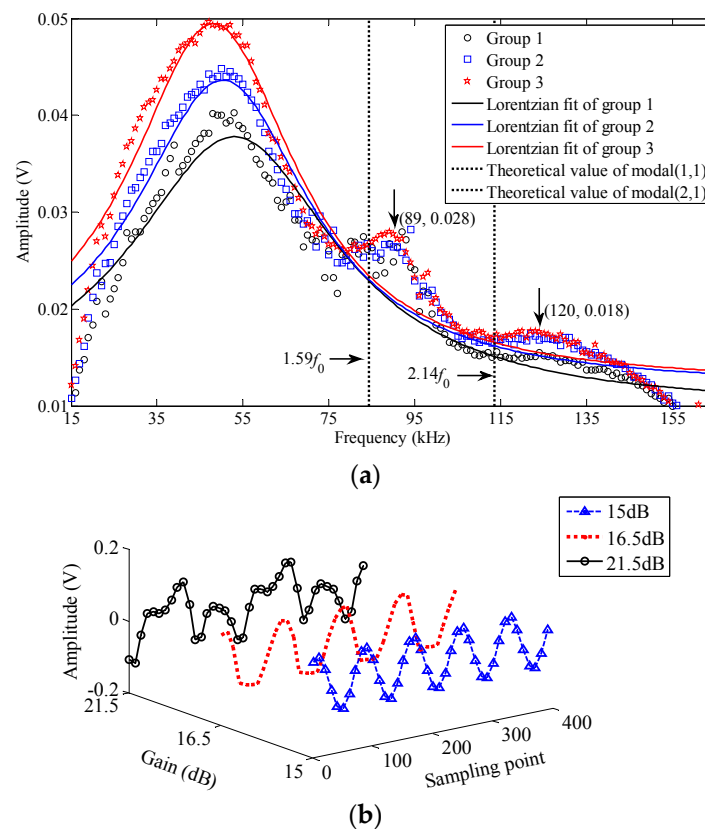


**Figure 6.** (a) Measured resonance spectrum and (b) nonlinear distortion due to increasing optical power at  $0^\circ\text{C}$ .

To sum up, the experimental results demonstrate that a simple and miniature optical fiber F-P resonator with MoS<sub>2</sub> or other 2D diaphragms can be successfully fabricated and tested instead of using a complicated free-space optical actuation scheme. However, when the resonator operates in air, its  $Q$  factor will be significantly reduced by viscous damping dissipation. Although a lower  $Q$  factor is weakly dependent on fundamental frequencies in the tested frequency range, its fluctuating change is quite significant with respect to the narrow bandwidth of about 40 kHz. It should be pointed out that the resonant frequency does not exhibit monotonic change with the temperature.



In fact, there appears to be an extremely low inflection point in the predicted spectrum due to internal thermal deformation on the membrane. The measured resonant frequencies differ from theoretical ones primarily because of the presence of non-uniformly distributed adsorbates, absorbed on the MoS<sub>2</sub> membranes in air. Unfortunately, the adsorbates result in additional masses and tensions, which will even cause the dispersion of resonant responses for different samples. Hence, the damping mechanism-dependent Knudsen number should be regulated optimally with the trade-off of sensitive structures of F-P resonators and testing conditions including temperature and pressure. In this case, the experimental results explain the low *Q*-factors of 2D nanomechanical resonators due to viscous air damping, which contributes to the sensitive structural optimization and packaging design of F-P resonators. Further research on the sensitive structural improvement of F-P resonators is needed to reduce air damping, in consideration of membrane size effect and optical fiber interference actuation.

#### 4. Conclusions

This study demonstrated a new type of mechanical F-P resonator based on a 125- $\mu$ m diameter nanothick suspended MoS<sub>2</sub> diaphragm using optical interference excitation and detection. Air damping effects on resonance behavior were experimentally investigated in the temperatures ranging from  $-10$  °C to  $80$  °C. Due to the interaction with the air, the MoS<sub>2</sub> device exhibited noticeable resonances with a maximum *Q* factor of  $\sim 1.35$  at  $0$  °C. Based on the derived viscous damping analytical model concerned with the Knudsen number, we identified the temperature-dependent modal frequencies from 36 kHz to 73 kHz, whose variation was described well with the result obtained by theoretical thermal expansion coefficients of MoS<sub>2</sub> reported in the previous study. By examining higher order modes, a qualitative description of measured nonlinear resonances was proposed through the dependence of photothermal excitation in its temperature. The experimental results shed light on the resonance behavior observed in 2D nanomechanical resonators in viscous air damping, which also contributes to the resonating performance optimization of F-P resonators with 2D diaphragm.

**Acknowledgments:** This work is supported by the National Nature Science Fund of China (61573033), the Aviation Science Foundation of China (20152251018), the Graduate Innovation Fund of Beihang University (YCSJ-01-2016-04, YCSJ-01-2016-05), and China Scholarship Council. We thank Ruitao Lv and Feifan Yu at Tsinghua University, China for the fabrication of MoS<sub>2</sub> membrane.

**Author Contributions:** Yumei She and Cheng Li conceived and designed the experiments, and then wrote the paper; Tian Lan performed the experiments; Qianwen Liu fabricated the F-P resonator using MoS<sub>2</sub> diaphragm; Xiaobin Peng analyzed the data; Shangchun Fan contributed materials/analysis tools.

**Conflicts of Interest:** The authors declare no conflict of interest.

#### References

1. Craighead, H.G. Nanoelectromechanical systems. *Science* **2000**, *290*, 1532–1535. [[CrossRef](#)] [[PubMed](#)]
2. Sage, E.; Brenac, A.; Alava, T.; Morel, R.; Dupre, C.; Hanay, M.S.; Roukes, M.L.; Duraffourg, L.; Masselon, C.; Hentz, S. Neutral particle mass spectrometry with nanomechanical systems. *Nat. Commun.* **2015**, *6*, 6482. [[CrossRef](#)] [[PubMed](#)]
3. Lassagne, B.; Tarakanov, Y.; Kinaret, J.; Sanchez, D.G.; Bachtold, A. Coupling mechanics to charge transport in carbon nanotube mechanical resonators. *Science* **2009**, *325*, 1107–1110. [[CrossRef](#)] [[PubMed](#)]
4. LaHaye, M.D.; Buu, O.; Camarota, B.; Schwab, K.C. Approaching the quantum limit of a nanomechanical resonator. *Science* **2004**, *304*, 74–77. [[CrossRef](#)] [[PubMed](#)]
5. Lee, J.S.; Wang, Z.H.; He, K.L.; Shan, J.; Feng, P.X.-L. Air damping of atomically thin MoS<sub>2</sub> nanomechanical resonators. *Appl. Phys. Lett.* **2014**, *105*, 023104. [[CrossRef](#)]
6. Liu, C.H.; Kim, I.S.; Lauhon, L.J. Optical control of mechanical mode-coupling within a MoS<sub>2</sub> resonator in the strong-coupling regime. *Nano Lett.* **2015**, *15*, 6727–6731. [[CrossRef](#)] [[PubMed](#)]
7. Bunch, J.S.; Van der Zande, A.M.; Verbridge, S.S.; Frank, I.W.; Tanenbaum, D.M.; Parpia, J.M.; Craighead, H.G.; McEuen, P.L. Electromechanical resonators from graphene sheets. *Science* **2007**, *315*, 490–493. [[CrossRef](#)] [[PubMed](#)]

8. Chen, C.Y.; Rosenblatt, S.; Bolotin, K.I.; Kalb, W.; Kim, P.; Kymissis, I.; Stormer, H.L.; Heinz, T.F.; Hones, J. Performance of monolayer graphene nanomechanical resonators with electrical readout. *Nat. Nanotechnol.* **2009**, *267*, 861–867. [[CrossRef](#)] [[PubMed](#)]
9. Van der Zande, A.M.; Barton, R.A.; Alden, J.S.; Ruiz-Vargas, C.S.; Whitney, W.S.; Pham, P.H.Q.; Park, J.; Parpia, J.M.; Craighead, H.G.; McEuen, P.L. Large-scale arrays of single-layer graphene resonators. *Nano Lett.* **2008**, *10*, 4869–4873. [[CrossRef](#)] [[PubMed](#)]
10. Barton, R.A.; Ilic, B.; Van der Zande, A.M.; Whitney, W.S.; McEuen, P.L.; Parpia, J.M.; Craighead, H.G. High, size-dependent quality factor in an array of graphene mechanical resonators. *Nano Lett.* **2011**, *11*, 1232–1236. [[CrossRef](#)] [[PubMed](#)]
11. Xu, H.T.; He, D.W.; Fu, M.; Wang, W.S.; Wu, H.P.; Wang, Y.S. Optical identification of MoS<sub>2</sub>/graphene heterostructure on SiO<sub>2</sub>/Si substrate. *Opt. Express* **2014**, *22*, 15969–15974. [[CrossRef](#)] [[PubMed](#)]
12. Philipp, T.; Robert, S.; Philipp, B.; Xiao, Z.; Janna, B.; Andreas, L.; Manfred, A.; Christian, K.; Ovidiu, G.; Dietrich, R.T.Z.; et al. Photoluminescence emission and Raman response of monolayer MoS<sub>2</sub>, MoSe<sub>2</sub>, and WSe<sub>2</sub>. *Opt. Express* **2013**, *21*, 4908–4916.
13. Jiang, J.W.; Park, H.S.; Rabczuk, T. MoS<sub>2</sub> nanoresonators: intrinsically better than graphene? *Nanoscale* **2014**, *6*, 3618–3625. [[CrossRef](#)] [[PubMed](#)]
14. Bertolazzi, S.; Brivio, J.; Kis, A. Stretching and breaking of ultrathin MoS<sub>2</sub>. *ACS Nano* **2011**, *5*, 9703–9709. [[CrossRef](#)] [[PubMed](#)]
15. Samanta, C.; Yasasvi Gangavarapu, P.R.; Naik, A.K. Nonlinear mode coupling and internal resonances in MoS<sub>2</sub> nanoelectromechanical system. *Appl. Phys. Lett.* **2015**, *107*, 173110. [[CrossRef](#)]
16. Lee, J.; Wang, Z.; He, K.; Shan, J.; Feng, P.X.-L. High frequency MoS<sub>2</sub> nanomechanical resonators. *ACS Nano* **2013**, *7*, 6086–6091. [[CrossRef](#)] [[PubMed](#)]
17. Castellanos-Gomez, A.; van Leeuwen, R.; Buscema, M.; van der Zant, H.S.J.; Steele, G.A.; Venstra, W.J. Single-layer MoS<sub>2</sub> mechanical resonators. *Adv. Mater.* **2013**, *25*, 6719–6723. [[CrossRef](#)] [[PubMed](#)]
18. Kramer, E.; van Dorp, J.; van Leeuwen, R.; Venstra, W.J. Strain-dependent damping in nanomechanical resonators from thin MoS<sub>2</sub> crystals. *Appl. Phys. Lett.* **2015**, *107*, 091903. [[CrossRef](#)]
19. Lee, J.; Krupcale, M.J.; Feng, P.X.-L. Effects of  $\gamma$ -ray radiation on two-dimensional molybdenum disulfide (MoS<sub>2</sub>) nanomechanical resonators. *Appl. Phys. Lett.* **2016**, *108*, 023106. [[CrossRef](#)]
20. Verbridge, S.S.; Ilic, R.; Craighead, H.G.; Parpia, J.M. Size and frequency dependent gas damping of nanomechanical resonators. *Appl. Phys. Lett.* **2008**, *93*, 013101. [[CrossRef](#)]
21. Liu, K.K.; Zhang, W.J.; Lee, Y.H.; Lin, Y.C.; Lin, Y.C.; Chang, M.T.; Su, C.Y.; Chang, C.S.; Li, H.; Shi, Y.; et al. Growth of large-area and highly crystalline MoS<sub>2</sub> thin layers on insulating substrates. *Nano Lett.* **2012**, *12*, 1538–1544. [[CrossRef](#)] [[PubMed](#)]
22. Rao, Y.J.; Wang, X.J.; Zhu, T.; Zhou, C.X. Demodulation algorithm for spatial-frequency-division-multiplexed fiber-optic Fizeau strain sensor networks. *Opt. Lett.* **2006**, *31*, 700–702. [[CrossRef](#)] [[PubMed](#)]
23. Li, C.; Xiao, J.; Guo, T.T.; Fan, S.C.; Jin, W. Interference characteristics in a Fabry–Perot cavity with graphene membrane for optical fiber pressure sensors. *Microsyst. Technol.* **2015**, *21*, 2297–2306. [[CrossRef](#)]
24. Bhiladvala, R.B.; Wang, Z.J. Effect of fluids on the Q factor and resonance frequency of oscillating micrometer and nanometer scale beams. *Phys. Rev. E* **2004**, *69*, 287–316. [[CrossRef](#)] [[PubMed](#)]
25. Singh, V.; Sengupta, S.; Solanki, H.S.; Dhall, R.; Allain, A.; Dhara, S.; Pant, P.; Deshmukh, M.M. Probing thermal expansion of graphene and modal dispersion at low-temperature using graphene nanoelectromechanical systems resonators. *Nanotechnology* **2010**, *21*, 165204–165211. [[CrossRef](#)] [[PubMed](#)]
26. Huang, L.F.; Gong, P.L.; Zeng, Z. Correlation between structure, phonon spectra, thermal expansion, and thermomechanics of single-layer MoS<sub>2</sub>. *Phys. Rev. B* **2014**, *90*, 716–723. [[CrossRef](#)]
27. Kwak, M.K. Vibration of circular membranes in contact with water. *J. Sound Vib.* **1994**, *178*, 688–690. [[CrossRef](#)]
28. Li, C.; Liu, Q.W.; Peng, X.B.; Fan, S.C. Analyzing the temperature sensitivity of Fabry–Perot sensor using multilayer graphene diaphragm. *Opt. Express* **2015**, *23*, 27494–27502. [[CrossRef](#)]
29. Vignola, J.F.; Judge, J.A.; Jarzynski, J.; Zalalutdinov, M.; Houston, B.H.; Baldwin, J.W. Effect of viscous loss on mechanical resonators designed for mass detection. *Appl. Phys. Lett.* **2006**, *88*, 041921. [[CrossRef](#)]

